AIAA 2016-2972
Aeroacoustics Conferences
30 May - 1 June, 2016, Lyon, France
22nd AIAA/CEAS Aeroacoustics Conference

A flux reconstruction technique for non-conforming grid interfaces in aeroacoustic simulations

S. Le Bras*
Centre Européen de Recherche et de Formation Avancée en Calcul Scientifique, 31057 Toulouse, France

H. Deniau†
ONERA, French Aerospace Lab, 31000 Toulouse, France

C. Bogey‡
Laboratoire de Mécanique des Fluides et d'Acoustique, Ecole Centrale de Lyon, Université de Lyon, 69134 Ecully, France.

In this study, a technique of flux reconstruction is proposed to perform aeroacoustic computations using high-order methods on multiblock structured meshes with non-conforming grid interfaces. The use of such grids facilitates zonal mesh refinements, and flows at high Reynolds numbers can thus be simulated at a reasonable cost. The high-order methods consists of low-dissipation and low-dispersion implicit finite-volume numerical schemes. Using a flux reconstruction method, they can be applied on non-conforming grids. In a first part, the method is described. It is based on the application of non-centered spatial schemes and the use of ghost cells. The flow variables in the ghost cells are computed from the flow field in the grid cells using local meshless interpolations with radial basis functions. Then, the performance of the method is evaluated by carrying out two-dimensional simulations of vortex convection and of a mixing layer. The results show that no significant spurious acoustic waves are produced at the grid interfaces. Finally, the flux reconstruction approach is applied to the computation of a three-dimensional jet at a Mach number of 0.6 and a Reynolds number based on the jet diameter of 5.7×10^5. In particular, non-conforming grids are used to obtain 384 points in the azimuthal discretization in the jet shear layers, while using less points at the center of the jet. Preliminary results regarding the jet development are shown and compared with experimental data.

I. Introduction

The direct computation of sound from the governing Navier-Stokes equations is an attractive way to study the noise generation mechanisms in turbulent flows and to design noise reduction devices. For flows at high Reynolds numbers, one of the main difficulties of such simulations is to deal with the large disparities between the fine-scale turbulent motions and the large wavelengths of the radiated noise. Consequently, local mesh refinements are needed to capture the small eddies generating noise, yielding severe numerical constraints. This is particularly true for turbofan jet flows at Reynolds numbers $Re_D > 10^6$, where D is the jet diameter. For such flows, the nozzle geometry is generally included in the simulations in order to obtain jet initial conditions as close as possible to those encountered in experiments. At high Reynolds numbers, very fine grids are therefore needed to compute a part of the boundary layer inside the nozzle and the jet shear layers. Usually, multiblock structured solvers are used, considering conforming grids with point-matched block interfaces as represented in Fig. 1(a). In this case, the zonal mesh refinements result in unnecessary very small mesh cells in certain flow regions, in particular at the center of the jet. Using explicit temporal

*Corresponding author. *Email address*: lebras@cerfacs.fr
†ONERA Research Scientist.
‡CNRS Research Scientist.

integration schemes, the presence of such mesh cells deteriorates the computational efficiency by imposing very small time steps verifying the CFL restriction. In addition, the prolongation of useless grid refinements increases the number of mesh points leading to extra costs. In this context, aeroacoustic simulations of jet flows at high Reynolds numbers is overly expensive. For complex geometries, the limitations mentioned above are so restrictive that in most cases the mesh cannot be built for structured conforming grids.

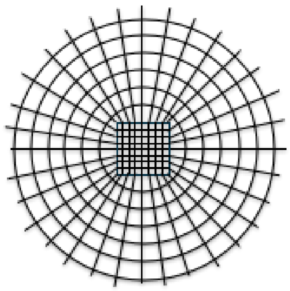

(a)

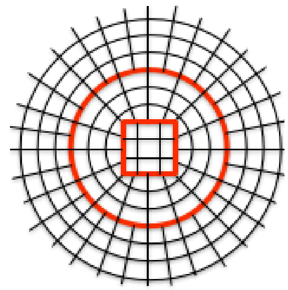

(b)

Fig. 1: Representation of a two-dimensional mesh with (a) conforming grid interfaces and (b) non-conforming grid interfaces in red.

In order to simulate flows at high Reynolds numbers, one solution is to use non-conforming grids which do not overlap each other. For such grids, the mesh lines can be discontinuous at the block interfaces. Figure 1(b) shows a typical non-conforming grid where the mesh spacing changes by a factor 2 in the azimuthal direction across the block interface colored in red. In this way, useless mesh refinements can be avoided. The size of the smallest cells and thus the time step can also be chosen such that the simulation is performed at a reasonable restitution time. In addition, the use of non-conforming grids offers some advantages in terms of grid generation. The meshes for the different elements or zones of the computational domain can be created independently and then easily assembled.

In aeroacoustic simulations, accurate numerical methods are required to capture the sound sources due to turbulent fluctuations and to propagate the generated acoustic waves in the far-field. In particular, the use of high-order low-dissipation and low-dispersion schemes ensures the resolution of the flows over a wide range of length scales in time and space. In the present study, a flux reconstruction technique is therefore proposed to properly use such schemes on non-conforming grids. The technique is implemented for 6th-order finite-volume compact schemes. It is based on the combination of non-centered schemes with local interpolations in order to reconstruct ghost cells and flux values at the grid interfaces. The interpolation method relies on a meshless approach involving radial basis functions.[1,2] Such interpolations are particularly interesting when using non-conforming grids in order to alleviate the difficulties caused by the loss of the mesh topology at the interfaces. Indeed, they are performed from arbitrarily scattered spatial data without any geometrical information, avoiding the computational overheads due to topology reconstructions. In this paper, in a first part, the flow solver and the flux reconstruction method are presented. In a second part, the performance of the reconstruction is examined by performing two-dimensional simulations of vortex convection and of a mixing layer. An application to a 3-D turbulent jet flow is also presented.

II. Numerical methods

A. Flow solver

1. *Governing equations*

The three-dimensional compressible Navier-Stokes equations are solved. Using Cartesian coordinates, they can be written in the following way:

$$\frac{\partial \mathbf{U}}{\partial t} + \frac{\partial \mathbf{E}_c}{\partial x} + \frac{\partial \mathbf{F}_c}{\partial y} + \frac{\partial \mathbf{G}_c}{\partial z} - \frac{\partial \mathbf{E}_d}{\partial x} - \frac{\partial \mathbf{F}_d}{\partial y} - \frac{\partial \mathbf{G}_d}{\partial z} = 0 \quad (1)$$

where $\mathbf{U} = (\rho, \rho u, \rho v, \rho w, \rho e)^t$ is the vector of the conservative variables, ρ is the density, $(u,\ v,\ w)$ are the velocity components, and ρe is the total energy. The terms $\mathbf{E}_c$, $\mathbf{F}_c$ and $\mathbf{G}_c$ are the convective fluxes, and the terms $\mathbf{E}_d$, $\mathbf{F}_d$ and $\mathbf{G}_d$ are the diffusive fluxes. For a perfect gas, the total energy ρe is given by:

$$\rho e = \frac{p}{\gamma - 1} + \frac{1}{2}\rho(u^2 + v^2 + w^2) \tag{2}$$

where p is the static pressure and γ is the specific heat ratio. The convective fluxes are defined by:

$$\begin{cases} \mathbf{E}_c = (\rho u, \rho u^2 + p, \rho uv, \rho uw, (\rho e + p)u)^t \\ \mathbf{F}_c = (\rho v, \rho uv, \rho v^2 + p, \rho vw, (\rho e + p)v)^t \\ \mathbf{G}_c = (\rho w, \rho uw, \rho vw, \rho w^2 + p, (\rho e + p)w)^t \end{cases} \tag{3}$$

and the diffusive fluxes by:

$$\begin{cases} \mathbf{E}_d = (0, \tau_{11}, \tau_{12}, \tau_{13}, \tau_{11}u + \tau_{12}v + \tau_{13}w + \Phi_1)^t \\ \mathbf{F}_d = (0, \tau_{21}, \tau_{22}, \tau_{23}, \tau_{21}u + \tau_{22}v + \tau_{23}w + \Phi_2)^t \\ \mathbf{G}_d = (0, \tau_{31}, \tau_{32}, \tau_{33}, \tau_{31}u + \tau_{32}v + \tau_{33}w + \Phi_3)^t \end{cases} \tag{4}$$

where τ_{ij} is the viscous stress tensor, and $\mathbf{\Phi} = (\Phi_1, \Phi_2, \Phi_3)^t$ is the heat flux vector. The viscous stress tensor τ_{ij} is defined by $\tau_{ij} = 2\mu S_{ij}$, where μ is the dynamic molecular viscosity computed from Sutherland's law and S_{ij} is the deformation stress tensor:

$$S_{ij} = \frac{1}{2}\left(\frac{\partial u_i}{\partial x_j} + \frac{\partial u_j}{\partial x_i} - \frac{2}{3}\frac{\partial u_k}{\partial x_k}\delta_{i,j}\right) \tag{5}$$

The heat flux vector $\mathbf{\Phi}$ is computed from Fourier's law, yielding:

$$\mathbf{\Phi} = -\lambda \nabla T \tag{6}$$

where ∇T is the temperature gradient, $\lambda = C_p\mu/Pr$ is the thermal conductivity, C_p is the specific heat at constant pressure, and Pr is the Prandtl number.

2. *High-order discretization in a finite-volume approach*

The computations are carried out using the ***elsA*** software,[3] which is a finite-volume multiblock structured solver. Direct Numerical Simulatons (DNS) or Large-Eddy Simulations (LES) can be performed. In DNS, all the turbulent scales are calculated. In LES, only the large turbulent flow scales are computed, whereas the effects of the small structures are taken into account by a subgrid-scale model. In a finite-volume approach, the Navier-Stokes equations are integrated over the control volumes of the mesh. For brevity and clarity, the method is presented for the linear convection equation:

$$\frac{\partial \mathbf{U}}{\partial t} + \nabla \cdot \mathbf{f}(\mathbf{U}) = 0 \tag{7}$$

where $\mathbf{f}$ is a vectorial function of $\mathbf{U}$. Equation (7) is integrated on the computational volume Ω_i using the divergence theorem:

$$\frac{d}{dt}\int_{\Omega_i} \mathbf{U} dV + \int_{\partial\Omega_i} \mathbf{f}(\mathbf{U}) \cdot \mathbf{n}\, dS = 0 \tag{8}$$

where $\partial\Omega_i$ corresponds to the faces of Ω_i, and $\mathbf{n}$ is the outgoing unitary normal of Ω_i. Using the linearity of $\mathbf{f}$ and supposing that the cells are hexahedrons, Eq. (8) is equivalent to:

$$\frac{d}{dt}\int_{\Omega_i} \mathbf{U} dV + \mathbf{f}\left(\int_{\partial\Omega_i} \mathbf{U} dS\right) \cdot \mathbf{n} = 0 \tag{9}$$

The calculation of the derivatives of $\mathbf{f}$ is replaced in Eq. (9) by the computation of $\mathbf{f}$ from the mean values of $\mathbf{U}$ at the cell interfaces. For this purpose, a monodimensional scheme is used. In the following, considering the one-dimensional domain of Fig.2, the mean value of $\mathbf{U}$ at the interface $I_{i+1/2}$ is given by:

$$\widetilde{\mathbf{U}}_{i+1/2} = \frac{1}{|I_{i+1/2}|}\int_{I_{i+1/2}} \mathbf{U} dS \tag{10}$$

and the mean value of $\mathbf{U}$ in the volume Ω_i by:

$$\overline{\mathbf{U}}_i = \frac{1}{|\Omega_i|} \int_{\Omega_i} \mathbf{U} dV \tag{11}$$

For the computation of the convective fluxes, the vector $\widetilde{\mathbf{U}}_{i+1/2}$ is obtained using the 6th-order implicit scheme of Fosso *et al.*:[4]

$$\alpha_{i+1/2}\widetilde{\mathbf{U}}_{i-1/2} + \widetilde{\mathbf{U}}_{i+1/2} + \beta_{i+1/2}\widetilde{\mathbf{U}}_{i+3/2} = \sum_{l=-1}^{2} a_l \overline{\mathbf{U}}_{i+l} \tag{12}$$

where $\alpha_{i+1/2}$, $\beta_{i+1/2}$ and a_l are the scheme coefficients.

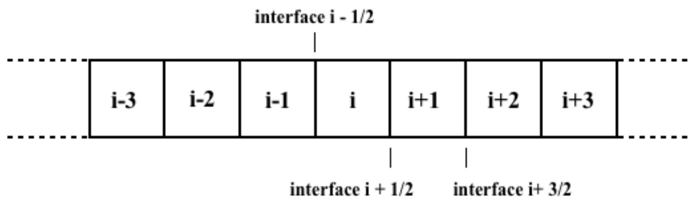

Fig. 2: Representation of a one-dimensional computational domain.

In order to ensure the stability of the centered scheme (12), the 6th-order compact filter of Visbal and Gaitonde[5] is applied to the flow variables in order to remove grid-to-grid oscillations. The filter is also used as a LES subgrid-scale model, dissipating turbulent energy at high frequencies.[6–8] It is employed on a uniformly spaced grid thanks to a coordinate transform. The filtered values, denoted $\widehat{\mathbf{U}}$, are estimated from the mean values $\overline{\mathbf{U}}$ as:

$$\alpha_f \widehat{\mathbf{U}}_{i-1} + \widehat{\mathbf{U}}_i + \alpha_f \widehat{\mathbf{U}}_{i+1} = \sum_{l=0}^{3} \frac{\gamma_l}{2} \left(\overline{\mathbf{U}}_{i+l} + \overline{\mathbf{U}}_{i-l} \right) \tag{13}$$

where $\alpha_f = 0.47$, and γ_l are the filter coefficients.[5] The diffusive fluxes in Eq. (4) are calculated from the gradient $\nabla\mathbf{U}$ estimated at the cell interfaces using a 2nd-order method.[9] For time discretization, a low-storage 6-stage Runge Kutta algorithm[10] is used. Radiation boundary conditions, Navier-Stokes characteristic boundary conditions as well as sponge zones are implemented in order to avoid significant acoustic reflections at the computational boundaries. A full description of the numerical algorithm is given in Fosso *et al.*[11]

B. Spatial discretization at the block interfaces

1. *Conforming grid interfaces*

At the interfaces between the mesh blocks, the 4-point scheme (12) cannot be applied. Therefore, for conforming grids, Fosso *et al.*[4] proposed a flux reconstruction at the interfaces. It consists in using a non-centered scheme to determine the values of $\widetilde{\mathbf{U}}$ at the interfaces, and thus compute the convective fluxes. The flux reconstruction technique is described for a two-dimensional computational domain composed of two blocks L and R separated by an interface as illustrated in Fig. 3. The procedure consists in two steps:

1. In the first step, in the block L, the variable vector $\widetilde{\mathbf{U}}_{N+1/2,j}$ at the interface I_L represented in red in Fig. 3(a) is computed using an upwind scheme. The scheme needs two cells (squares) and an interface (cross) in the block L, and two ghost cells (stars) in the block R as:

$$\alpha'_{N+1/2}\widetilde{\mathbf{U}}_{N-1/2,j} + \widetilde{\mathbf{U}}_{N+1/2,j} = \underbrace{a'_0\overline{\mathbf{U}}_{i=N-l,j} + a'_1\overline{\mathbf{U}}_{i=N,j}}_{\text{cells of block L}} + \underbrace{a'_2\overline{\mathbf{U}}_{i'=0,j} + a'_3\overline{\mathbf{U}}_{i'=1,j}}_{\text{cells of block R}} \tag{14}$$

where $\alpha'_{N+1/2}$ and a'_i are the upwind scheme coefficients which are determined using Taylor series. Data exchanges between the blocks at each time step during the simulation allow the values of $\overline{\mathbf{U}}_{i'=0,j}$

and $\overline{\mathbf{U}}_{i'=1,j}$ to be known in the block L. In the block R, the vector $\widetilde{\mathbf{U}}_{-1/2,j}$ at the interface I_R in blue in Fig. 3(b) is computed similarly:

$$\widetilde{\mathbf{U}}_{-1/2,j} + \beta''_{-1/2}\widetilde{\mathbf{U}}_{1/2,j} = \underbrace{a''_0\overline{\mathbf{U}}_{i=N-1,j} + a''_1\overline{\mathbf{U}}_{i=N,j}}_{\text{cells of block L}} + \underbrace{a''_2\overline{\mathbf{U}}_{i'=0,j} + a''_3\overline{\mathbf{U}}_{i'=1,j}}_{\text{cells of block R}} \tag{15}$$

where $\beta''_{-1/2}$ and a''_i are the scheme coefficients.

2. The values of $\widetilde{\mathbf{U}}$ obtained at the interfaces I_L and I_R usually differ from each other since they are estimated from the upwind schemes (14) and (15). Therefore, in the second step, the unicity of the flux at the block interface is ensured by the resolution of the Riemann problem.[12]

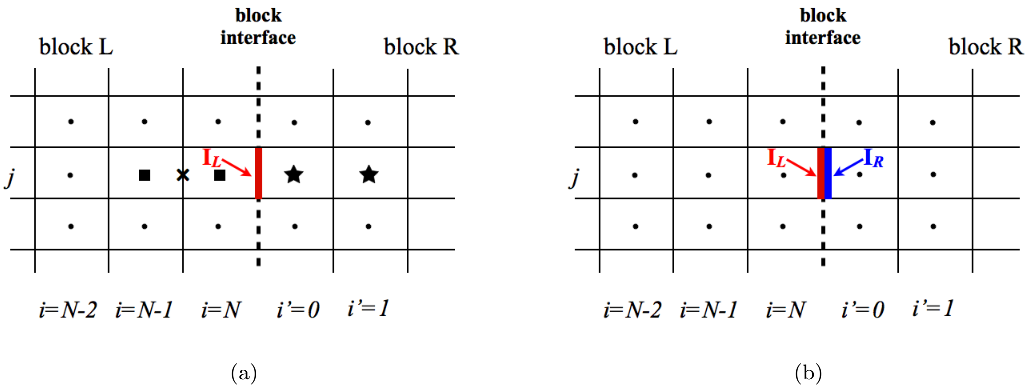

Fig. 3: Flux reconstruction for conforming grids: (a) step 1: computation of the flow field variables at the block interface I_L using a non-centered scheme involving two cells (squares) and an interface (cross) in the block L and two ghost cells (stars) in the block R, (b) step 2: computation of the flux from the flow variables at the interfaces I_L (red) and I_R (blue), using a Riemann solver.

As for the scheme of Fosso et al.,[4] a specific procedure has also been developed[13] to apply the 7-point filter of Visbal and Gaitonde[5] near conforming grid interfaces. It consists in using the centered filter (13) and five ghost cells indexed by $i' = 0, 1, 2, 3, 4$ in Fig. 3. Previous studies[13] demonstrated that the application of the filter in ghost cells is particularly interesting in order to avoid a significant decrease of the spectral accuracy of the 6th-order filter of Visbal and Gaitonde[5] near the block interfaces. In Fig. 3, close to the interface in block L, relation (13) is applied until the ghost cell $(i' = 1, j)$ as:

$$\alpha_f\widehat{\mathbf{U}}_{i'=0,j} + \widehat{\mathbf{U}}_{i'=1,j} + \alpha_f\widehat{\mathbf{U}}_{i'=2,j} = \sum_{k=2}^{3}\frac{\gamma_k}{2}\overline{\mathbf{U}}_{i=N-k+2,j} + \frac{\gamma_1}{2}\overline{\mathbf{U}}_{i'=0,j} + \gamma_0\overline{\mathbf{U}}_{i'=1,j} + \sum_{k=1}^{3}\frac{\gamma_k}{2}\overline{\mathbf{U}}_{i'=k+1,j} \tag{16}$$

Note that in Eq. (16), the filtered value $\widehat{\mathbf{U}}_{i'=2,j}$ is needed. It obtained assuming the flow field in the ghost cell $(i' = 2, j)$ is unfiltered, yielding:

$$\widehat{\mathbf{U}}_{i'=2,j} = \overline{\mathbf{U}}_{i'=2,j} \tag{17}$$

2. Non-conforming grid interfaces

For non-conforming grids, as shown in Fig. 4, the flux reconstruction technique presented above cannot be applied. Indeed, the upwind scheme (14) cannot be implemented since the ghost cells represented by stars in Fig. 3(a) are not defined when the mesh lines are discontinuous at the block interface. In this work, a new flux reconstruction is thus proposed at the non-conforming grid interfaces. Inspired by the technique previously presented for conforming grids, the method consists in defining ghost cells in order to apply scheme (14) and then compute the fluxes at the block interfaces. The approach, composed of four steps, is illustrated in Fig. 4 for the computation of the flux in the block L at the interface I_L represented in red.

1. First, in order to compute the flow variables $\widetilde{\mathbf{U}}_{N+1/2,j}$ at the interface I_L using scheme (14), two ghost cells indicated by stars in Fig. 4(a) are defined. The ghost cells are located in the planes $i' = 0$ and

$i' = 1$. They are found at the intersection between the plane $i' = 0$ or 1 and the straight line defined by the center of the cells $(i = N-1, j)$ and $(i = N, j)$. In the case of the conforming grid of Fig. 3(a), the ghost cell positions correspond to the centers of the cells $(i' = 0, j)$ and $(i' = 1, j)$ in the block R. The value of $\overline{\mathbf{U}}$ in the ghost cells is then calculated using the interpolation technique described in section II.C.1.

2. In a second step, as shown in Fig. 4(b), the upwind scheme (14) is used to compute the vector $\widetilde{\mathbf{U}}_{N+1/2,j}$ at the interface I_L.

3. Using the same methodology, in the block R, the vectors (..., $\widetilde{\mathbf{U}}_{-1/2,j'}$, $\widetilde{\mathbf{U}}_{-1/2,j'+1}$, ...) are computed at the interfaces (..., $I_{-1/2,j'}$, $I_{-1/2,j'+1}$, ...) in blue in Fig. 4(c).

4. The values of $\widetilde{\mathbf{U}}$ obtained in step 3 are finally employed to interpolate an equivalent variable vector $\widetilde{\mathbf{U}}_{-1/2,j}$ at the interface denoted I_R in Fig. 4(d). The interface I_R is geometrically identical to I_L. This second interpolation technique is presented in section II.C.2. Finally, the convective flux at the block interface is determined from the values of $\widetilde{\mathbf{U}}_{N+1/2,j}$ and $\widetilde{\mathbf{U}}_{-1/2,j}$ by resolving a Riemann flux problem.[12]

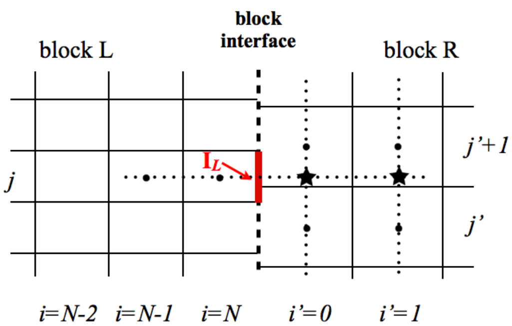

(a)

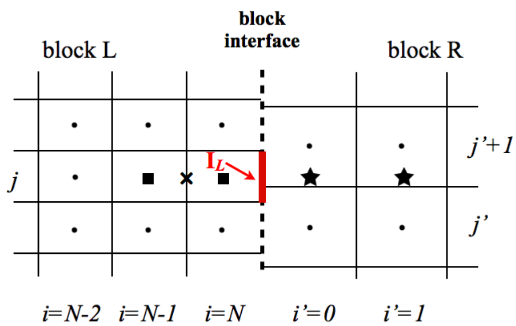

(b)

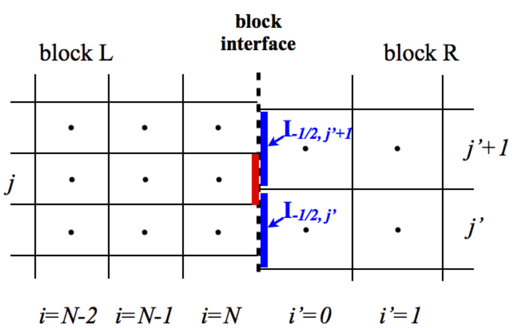

(c)

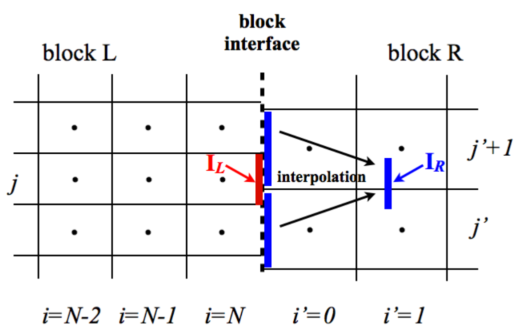

(d)

Fig. 4: Flux reconstruction for non-conforming grids at the interface I_L in block L: (a) step 1: definition of two ghost cells (stars), (b) step 2: computation of the flow variables at the interface I_L using a non-centered scheme, (c) step 3: computation of the flow variables at the interfaces in blue using a non-centered scheme, (d) step 4: interpolation of the flow variables at the interface I_R using the data computed in step 3, and computation of the resulting flux at the block interface using a Riemann solver.

Concerning the 6th-order filter of Visbal and Gaitonde,[5] five ghost cells are necessary to apply the relation (16) proposed for conforming grids. For such grids, the flow variables in the ghost cells are obtained thanks to data exchanges between blocks. However, for non-conforming grids, they are computed using interpolations. Consequently, the use of five ghost cells leads to an extra cost compared to conforming grids. Therefore, the number of ghost cells is limited to two. Using the notations of Fig. 4, in the block L, using two ghost cells, it is possible to implement the 7-point filter (13) until the point $(i = N-1, j)$. At the cell $(i = N, j)$ adjacent to the block interface, the filtered field $\widehat{\mathbf{U}}_{i=N,j}$ is computed from the upwind formulation:

$$\alpha_f \widehat{\mathbf{U}}_{i=N-1,j} + \widehat{\mathbf{U}}_{i=N,j} + \alpha_f \widehat{\mathbf{U}}_{i'=0,j} = \sum_{k=0}^{4} \gamma'_k \overline{\mathbf{U}}_{N-4+k,j} + \gamma'_5 \overline{\mathbf{U}}_{i'=0,j} + \gamma'_6 \overline{\mathbf{U}}_{i'=1,j} \tag{18}$$

The flow variables in the ghost cells $(i' = 0, j)$ and $(i' = 1, j)$ are also filtered using the non-centered relations:

$$\begin{cases} \alpha_f \widehat{\mathbf{U}}_{i=N,j} + \widehat{\mathbf{U}}_{i'=0,j} + \alpha_f \widehat{\mathbf{U}}_{i'=1,j} = \sum\limits_{k=0}^{4} \gamma''_k \overline{\mathbf{U}}_{N-4+k,j} + \gamma''_5 \overline{\mathbf{U}}_{i'=0,j} + \gamma''_6 \overline{\mathbf{U}}_{i'=1,j} \\ \alpha_f \widehat{\mathbf{U}}_{i'=0,j} + \widehat{\mathbf{U}}_{i'=1,j} = \sum\limits_{k=0}^{4} \gamma'''_k \overline{\mathbf{U}}_{N-4+k,j} + \gamma'''_5 \overline{\mathbf{U}}_{i'=0,j} + \gamma'''_6 \overline{\mathbf{U}}_{i'=1,j} \end{cases} \tag{19}$$

where $\alpha_f = 0.47$, and γ'_k, γ''_k and γ'''_k are the non-centered filters coefficients.[14]

C. Interpolation technique

In this section, the interpolation techniques used to compute the flow variables in the ghost cells and at the grid interfaces are described. Radial Basis Function (RBF) interpolations[1] are employed.

1. *Definition of the flow variables in the ghost cells*

The interpolation method used to reconstruct the flow variables $\overline{\mathbf{U}}$ in the ghost cell $(i' = 0, j)$ represented by a star in Fig. 5(a) is presented. The interpolation is performed from the values of $\overline{\mathbf{U}}$ in cells of the block R located in a area around the ghost cell. This area, represented in grey in Fig. 5, contains cell centers at $i' = 0$. More precisely, in Fig. 5(b), its size is defined by a radius $R_v = n_v r_{min}$, where n_v is a positive integer and r_{min} is the minimal distance between the ghost cell center and the points of the area. In the following, the position of the ghost cell is denoted $\mathbf{x} = (x, y, z)$ in Cartesian coordinates, the integer n_p is the number of points contained in the area, and the quantity u corresponds to a variable of vector $\overline{\mathbf{U}}$. The RBF interpolation consists in determining an approximation function $u(\mathbf{x})$ using the values of u known at the n_p points in the grey area.

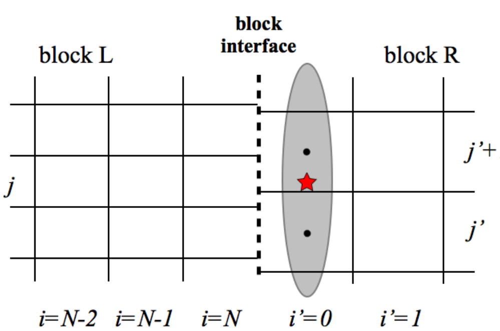

(a)

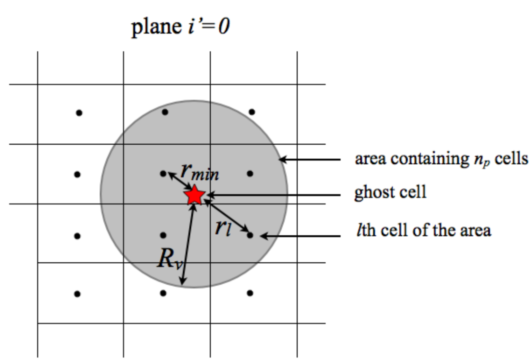

(b)

Fig. 5: Representation of the area (in grey) considered for the interpolation of the flow variables in the ghost cell $(i' = 0, j)$ indicated by a star: (a) in the plane (i, j) (b) in the plane $i' = 0$: r_l is the distance between the center of the ghost cell (star) and the center of the lth cell of the area, $R_v = n_v r_{min}$ is the radius of the grey area where $r_{min} = \min(r_l)$ and n_v is a positive integer.

The function $u(\mathbf{x})$ is defined as a linear combinaison of radial basis functions $\Phi_l(\mathbf{x})$ and polynomials $P_q(\mathbf{x})$:[2]

$$u(\mathbf{x}) = \sum_{l=1}^{n_p} \lambda_l \Phi_l(\mathbf{x}) + \sum_{q=1}^{m} \beta_q P_q(\mathbf{x}) \tag{20}$$

where λ_l and β_q are the unknown interpolation coefficients and m is the number of polynomial functions. In this study, Wendland's basis functions[2,15] with compact support are used:

$$\Phi_l(\mathbf{x}) = \Phi(r_l) = (1 - r_l)^4_+ (4r_l + 1) \qquad 1 \leq l \leq n_p \tag{21}$$

where r_l denotes the Euclidian distance between the point $\mathbf{x}$ and the node $\mathbf{x}_l$ in Fig. 5(b), and $(1-r_l)_+$ corresponds to:

$$(1-r_l)_+ = \begin{cases} (1-r_l) & \text{if } 0 \leq r_l \leq R_v \\ 0 & \text{if } r_l > R_v \end{cases} \tag{22}$$

The polynomial term in Eq. (20) is given by:

$$P^T(\mathbf{x}) = (1, x, y, z, x^2, xy, y^2, ...) \tag{23}$$

This term ensures that approximation (20) has a unique solution[1,16] by imposing the orthogonality constraints:

$$\sum_{l=1}^{n_p} P_q(\mathbf{x}_l)\lambda_l = 0 \quad \text{for } 1 \leq q \leq m \tag{24}$$

The coefficients λ_l and β_q are chosen so that the approximation $u(\mathbf{x})$ is exact for the n_p points contained in the grey area. Therefore, the interpolation formulation (20) satisfies the following relations:

$$u(\mathbf{x}_k) = u_k = \sum_{l=1}^{n_p} \lambda_l \Phi_l(\mathbf{x}_k) + \sum_{q=1}^{m} \beta_q P_q(\mathbf{x}_k) \quad \text{for } 1 \leq k \leq n_p \tag{25}$$

where u_k corresponds to the value of u at the kth point of the grey area. This value is supposed to be known. The values of λ_l and β_q are obtained by resolving the system:

$$\begin{pmatrix} \mathbf{\Phi} & \mathbf{P} \\ \mathbf{P}^T & \mathbf{0} \end{pmatrix} \begin{pmatrix} \boldsymbol{\lambda} \\ \boldsymbol{\beta} \end{pmatrix} = \begin{pmatrix} \mathbf{u}^{set} \\ \mathbf{0} \end{pmatrix} \tag{26}$$

where $\boldsymbol{\lambda} = (\lambda_1, ..., \lambda_{n_p})^T$ and $\boldsymbol{\beta} = (\beta_1, ..., \beta_m)^T$ are the vectors of the interpolation coefficients to be determined, $\mathbf{u}^{set} = (u_1, ..., u_{n_p})^T$, and $\mathbf{\Phi} \in \mathbb{R}^{n_p \times n_p}$ and $\mathbf{P} \in \mathbb{R}^{n_p \times m}$ are matrices defined from the basis functions by:

$$\begin{aligned} \mathbf{\Phi}_{kl} &= \Phi_l(\mathbf{x}_k) \quad && 1 \leq k, l \leq n_p \\ \mathbf{P}_{kq} &= P_q(\mathbf{x}_k) \quad && 1 \leq k \leq n_p \text{ and } 1 \leq q \leq m \end{aligned} \tag{27}$$

For the conforming grid interface of Fig. 3, the interpolated value $u(\mathbf{x})$ corresponds to the quantity u in the cell of block R located at $i' = 0$ and j. Indeed, in this case, the ghost cell is a grid cell of the grey area. Consequently, the interpolation is by definition exact from relation (25). Concerning the choice of the polynomial term (23), imposing $P^T(\mathbf{x}) = 1$ allows to preserve a uniform flow. For example, if u_k is equal to a constant C regardless of the value of k, $u(\mathbf{x}) = \beta_0 = C$ is the trivial solution to the interpolation problem (26). In the following, the interpolations will be performed using $P^T(\mathbf{x}) = 1$ or $P^T(\mathbf{x})=(1,\ x,\ y,\ z)$. Finally, the value of $\overline{\mathbf{U}}$ in the second ghost cell in Fig. 4(a) is reconstructed similarly, using n_p points in the plane $i' = 1$.

2. *Definition of the flow variables at the block interface*

As mentioned in section II.B.2, a second interpolation is performed to determine the vector $\widetilde{\mathbf{U}}_{-1/2,j}$ at the interface I_R shown in Fig. 4(d). The technique is similar to the one proposed for the flow definition in the ghost cells. However, the objective of this interpolation is to calculate a value of $\widetilde{\mathbf{U}}$ at the block interface instead of a discrete value of $\overline{\mathbf{U}}$. Therefore, the interpolation is performed from n_p vectors $(\widetilde{\mathbf{U}}_{-1/2,1}, ..., \widetilde{\mathbf{U}}_{-1/2,j'}, ..., \widetilde{\mathbf{U}}_{-1/2,n_p})$ at the interfaces $(I_{-1/2,1}, ..., I_{-1/2,j'}, ..., I_{-1/2,n_p})$ represented in blue in Fig. 4(c). As previously, the size of the area containing the n_p interfaces is set by the value of R_v. Once again, a reconstruction of u by a RBF interpolation is used:

$$u(\mathbf{x}) = \sum_{l=1}^{n_p} \lambda'_l \Phi_l(\mathbf{x}) + \sum_{q=1}^{m} \beta'_q P_q(\mathbf{x}) \tag{28}$$

where λ'_l et β'_q are the unknown coefficients. The variable $\tilde{u}_{-1/2,j}$ of the field $\widetilde{\mathbf{U}}_{-1/2,j}$ results from the integration of u on the interface I_R. Integrating relation (28) yields:

$$\begin{aligned}\tilde{u}_{-1/2,j} &= \frac{1}{|I_R|}\int_{I_R} u dS \\ &= \sum_{l=1}^{n_p}\lambda'_l\left(\frac{1}{|I_R|}\int_{I_R}\Phi(r_{jl})dS\right)+\sum_{q=1}^{m}\beta'_q\left(\frac{1}{|I_R|}\int_{I_R}P_q dS\right)\end{aligned} \tag{29}$$

where r_{jl} is the Euclidian distance between the center of the interface $I_{-1/2,l}$ and the current point of the interface I_R where the integral is estimated. The coefficients λ'_l et β'_q are determined by integrating the interpolation fonction (28) on the n_p interfaces $(I_{-1/2,1}, ..., I_{-1/2,j'}, ..., I_{-1/2,n_p})$, and by imposing that the integrals obtained correspond to the vectors $(\widetilde{\mathbf{U}}_{-1/2,1}, ..., \widetilde{\mathbf{U}}_{-1/2,j'}, ..., \widetilde{\mathbf{U}}_{-1/2,n_P})$. It yields for the interface $I_{-1/2,k}$:

$$\tilde{u}_{-1/2,k} = \sum_{l=1}^{n_p}\lambda'_l\left(\frac{1}{|I_{-1/2,k}|}\int_{I_{-1/2,k}}\Phi(r_{kl})dS\right)+\sum_{q=1}^{m}\beta'_q\left(\frac{1}{|I_{-1/2,k}|}\int_{I_{-1/2,k}}P_q dS\right) \quad \text{for } 1\le k\le n_p \tag{30}$$

where $\tilde{u}_{-1/2,k}$ is a component of the averaged field $\widetilde{\mathbf{U}}_{-1/2,k}$ at the interface $I_{-1/2,k}$. In practice, the coefficients λ'_l and β'_q are computed by the resolution of the system:

$$\begin{pmatrix}\mathbf{\Phi}' & \mathbf{P}' \\ \mathbf{P}'^T & \mathbf{0}\end{pmatrix}\begin{pmatrix}\boldsymbol{\lambda}' \\ \boldsymbol{\beta}'\end{pmatrix} = \begin{pmatrix}\tilde{\mathbf{u}}^{set} \\ \mathbf{0}\end{pmatrix} \tag{31}$$

where $\boldsymbol{\lambda}' = (\lambda'_1, ..., \lambda'_{n_p})^T$ and $\boldsymbol{\beta}' = (\beta'_1, ..., \beta'_m)^T$ are the vectors of the interpolation coefficients, $\tilde{\mathbf{u}}^{set} = (\tilde{u}_{-1/2,1}, ..., \tilde{u}_{-1/2,n_p})^T$, and $\mathbf{\Phi}' \in \mathbb{R}^{n_p\times n_p}$ and $\mathbf{P}' \in \mathbb{R}^{n_p\times m}$ are matrices defined from the basis functions by:

$$\begin{aligned}\mathbf{\Phi}'_{kl} &= \frac{1}{|I_{-1/2,k}|}\int_{I_{-1/2,k}}\Phi(r_{kl})dS \quad 1\le k,l\le n_p \\ \mathbf{P}'_{kq} &= \frac{1}{|I_{-1/2,k}|}\int_{I_{-1/2,k}}P_q dS \quad 1\le k\le n_p \text{ and } 1\le q\le m\end{aligned} \tag{32}$$

III. Numerical simulations

The performance of the flux reconstruction on non-conforming grids is evaluated by performing 2-D simulations of vortex convection and of a mixing layer on Cartesian meshes. The flux reconstruction is also applied in 3-D for a turbulent jet flow.

A. Convection of a vortex

1. Parameters

A round vortex is convected in a mean flow characterized by a Mach number M of 0.5, a pressure of 10^5 Pa and a temperature of 300 K. The bidimensional computational domain considered for the simulations extends from $x = 0$ down to $x = 3L$ in the streamwise direction, and from $y = 0$ up to $y = L$ in the transverse direction, where $L = 0.1$ m. It is divided in two blocks separated by a vertical non-conforming interface located at $x = L$. The vortex is defined by the velocity and pressure fluctuations:

$$\begin{cases} u' = -\dfrac{\Gamma}{R^2}(y-y_c)\exp\left(-\ln 2\dfrac{(x-x_c)^2+(y-y_c)^2}{2b^2}\right) \\ v' = \dfrac{\Gamma}{R^2}(x-x_c)\exp\left(-\ln 2\dfrac{(x-x_c)^2+(y-y_c)^2}{2b^2}\right) \\ p' = -\dfrac{\rho\Gamma^2}{2R^2}\exp\left(-\ln 2\dfrac{(x-x_c)^2+(y-y_c)^2}{b^2}\right)\end{cases} \tag{33}$$

where $(x_c = 0.5L, y_c = 0.5L)$ is the position of the vortex center at the initial time $t = 0$, $b = (\sqrt{\ln 2}/20)L \simeq 0.04L$ is the vortex half-width, $R = b/\sqrt{\ln 2}$, and Γ represents its intensity given by:

$$\frac{\rho \Gamma^2}{2R^2} = 10^3 \text{ Pa} \tag{34}$$

The velocity and pressure fluctuations are superimposed onto the mean flow at $t = 0$. The performance of the flux reconstruction at the interface is examined by performing four simulations using different meshes (see Fig. 6), with and without RBF interpolations. The grid parameters, namely the mesh spacings in the streamwise direction Δx, and in the transverse direction on the left and the right sides of the interface Δy^L and Δy^R, as well as the flux reconstruction technique at the block interface, are provided in Tab. 1.

simulation	Δx	Δy^L	Δy^R	flux reconstruction technique
Vo-RBF-Coarsegrid	Δ	Δ	2.0 Δ	RBF interpolations
Vo-RBF-Mediumgrid	Δ	Δ	1.5 Δ	RBF interpolations
Vo-RBF-Finegrid	Δ	Δ	1.3 Δ	RBF interpolations
Vo-noRBF-Mediumgrid	Δ	Δ	1.5 Δ	2nd-order interpolations

Table 1: Parameters of the simulations of the vortex convection: Δx is the mesh spacing in the streamwise direction, Δy^L and Δy^R are the mesh spacings in the transverse direction at the left and the right sides of the non-conforming grid interface, $\Delta = L/127$.

The influence of the spatial resolution on the flux reconstruction is evaluated by performing three simulations using different mesh spacings on the right side of the block interface. The simulations are denoted Vo-RBF-Coarsegrid, Vo-RBF-Mediumgrid, Vo-RBF-Finegrid. The three meshes close to the block interface are represented in Fig. 6. In all cases, in the streamwise direction, there is no discontinuity of the mesh lines at the block interface, and a constant grid spacing of $\Delta x = \Delta = L/127$ is applied. The vortex half-width b is thus discretized by 5 points ($b = 5.29\Delta$). In the transverse direction, on the left side of the interface, the grid spacing Δy^L is constant and also equal to Δ. On the right side of the interface, in order to obtain a non-conforming grid, a poorer mesh resolution is chosen in the y-direction. More precisely, the grid spacing Δy^R is respectively equal to 2Δ, 1.5Δ and 1.3Δ for the coarse, the medium and the fine grids, corresponding to a discretization of the vortex half-width by 2.6, 3.5 and 4 points. Concerning the flux reconstruction at the block interface, in Vo-RBF-Coarsegrid, Vo-RBF-Mediumgrid and Vo-RBF-Finegrid, RBF interpolations are carried out using points contained in an area defined by $n_v = 5$ and the polynomial function $P^T(\mathbf{x}) = 1$.

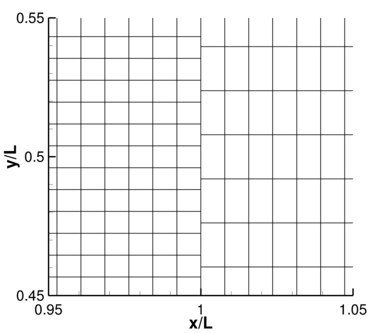

(a)

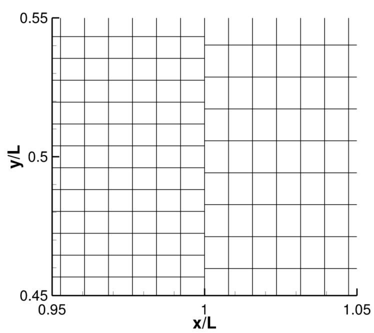

(b)

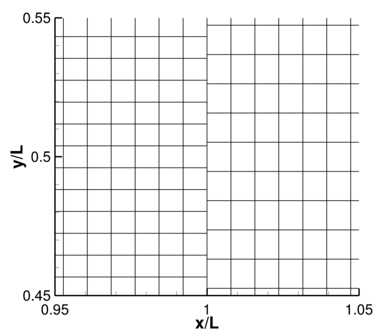

(c)

Fig. 6: Representation of the meshes close to the block interface: (a) Vo-RBF-Coarsegrid, (b) Vo-RBF-Mediumgrid and Vo-noRBF-Mediumgrid and (c) Vo-RBF-Finegrid.

The performance of the RBF interpolation technique is examined by performing a fourth simulation without RBF interpolation. The simulation is denoted Vo-noRBF-Mediumgrid. Its parameters are identical to those in Vo-RBF-Mediumgrid, except for the ghost cell definition and the flux reconstruction at the interface which are computed using 2nd-order interpolations. In this case, as shown in Fig. 7, the variable vector $\overline{\mathbf{U}}$ in the ghost cell $(i' = 0, j)$ delimited in red is defined as the weighted sum of $\overline{\mathbf{U}}$ in the cells of block R $(i' = 0, j')$ and $(i' = 0, j' + 1)$:

$$\overline{\mathbf{U}}_{i'=0,j} = \frac{|LM|}{|LN|}\overline{\mathbf{U}}_{i'=0,j'} + \frac{|MN|}{|LN|}\overline{\mathbf{U}}_{i'=0,j'+1} \tag{35}$$

The flow field in the ghost cell $(i' = 1, j)$ and the flux at the block interface are computed in a similar way.

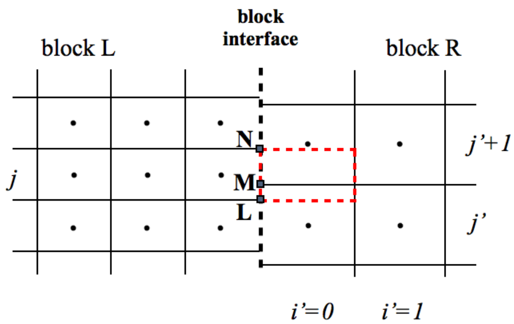

Fig. 7: Representation of a non-conforming grid where the interface LN is divided in two parts LM and MN. The flow variables in the ghost cell represented in red dashed line are calculated from the flow field in the computational cells $(i' = 0, j')$ and $(i' = 0, j' + 1)$.

The time step Δt in the computations is chosen in order to impose a CFL number $(1 + M)c\Delta t/\Delta$ of 0.2, where c is the sound speed. When the vortex crosses the block interface, numerical waves may be generated due to the difference in grid resolution as well as to the new spatial discretization at the interface. The objective is to ensure that the amplitude of these spurious waves is very low with respect to the pressure deficit in the vortex. Therefore, we propose to compare the pressure field $p_{\text{interface}}$ obtained in the multiblock simulations with the field $p_{\text{no-interface}}$ computed from simulations without block interface. In particular, four monoblock simulations are carried out using a mesh spacing Δy respectively equal to Δ, 1.3Δ, 1.5Δ and 2Δ in all the computational domain. The other parameters are similar to those in the simulations in Tab. 1. Comparing the pressure $p_{\text{interface}}$ with $p_{\text{no-interface}}$ instead of with the analytical vortex definition (33) is proposed in order to take into account the vortex discretization on the meshes.

2. Influence of the radial basis function interpolations

In this section, the performance of the RBF interpolations is investigated by comparing the results obtained in the simulations Vo-noRBF-Mediumgrid and Vo-RBF-Mediumgrid. Snapshots of the pressure field $\Delta p = p_{\text{interface}} - p_{\text{no-interface}}$ when the vortex is located at $x = 1.25L$ are displayed in Fig. 8. In all cases, a wave is generated when the vortex goes through the interface. The amplitude of Δp is of a few Pascal which is low compared to the pressure variations of 10^3 Pa at the center of the vortex. Stronger levels are obtained in Vo-noRBF-Mediumgrid using 2nd-order interpolations for the flux reconstruction at the block interface than in Vo-RBF-Mediumgrid using RBF interpolations.

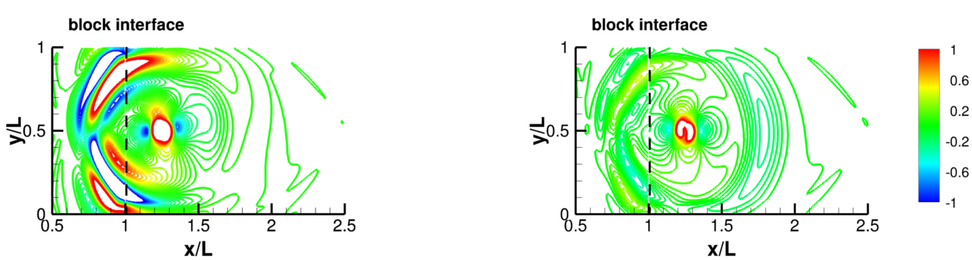

(a) (b)

Fig. 8: Representation of the pressure difference Δp when the vortex is located at $x = 1.25L$: (a) Vo-noRBF-Mediumgrid and (b) Vo-RBF-Mediumgrid; levels are given in Pa.

The time evolution of the pressure difference Δp is recorded at the three mesh points A, B, C indicated by squares in Fig. 9. They are located upstream the block interface at $x = 0.8L$ and $y = 0.75L$, at the interface at $x = L$ and $y = 0.5L$, and downstream the interface at $x = 1.2L$ and $y = 0.75L$, respectively. The signals at these points in Vo-noRBF-Mediumgrid and Vo-RBF-Mediumgrid are presented in Fig. 10. The maximum levels are found in Fig. 10(b) at the point B located at the interface. In Vo-noRBF-Mediumgrid, the pressure difference Δp at the points A, B and C reaches peaks of 1.5 Pa, -3.1 Pa and 0.8 Pa. In Vo-RBF-Mediumgrid, the levels are at least 60% lower than in the previous case, with maximum values of 0.3 Pa, 1.1 Pa and 0.2 Pa. These results demonstrate the advantage of using RBF interpolations for the spatial discretization at the block interface.

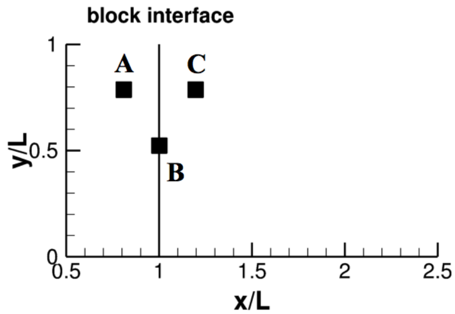

Fig. 9: Representation of the mesh points A, B and C (squares) where the pressure field is recorded.

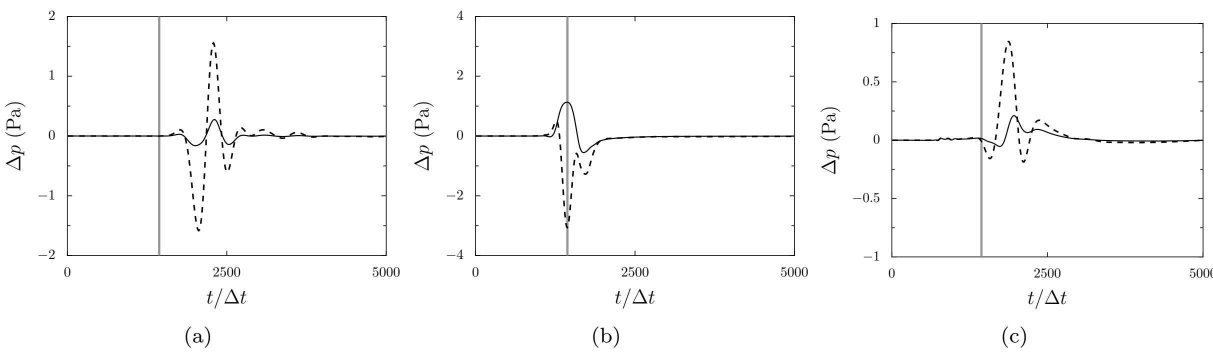

Fig. 10: Representation of the time evolution of the pressure difference Δp (a) at point A, (b) at point B and (c) at point C: – – – Vo-noRBF-Mediumgrid and —— Vo-RBF-Mediumgrid. The vertical grey line indicates the moment when the vortex hits the interface.

3. *Influence of the mesh resolution at the right side of the block interface*

Snapshots of the pressure difference Δp obtained in Vo-RBF-Coarsegrid, Vo-RBF-Mediumgrid and Vo-RBF-Finegrid are shown in Fig. 11. Increasing the mesh resolution in the y-direction on the right-hand side of the interface, using mesh spacings from $\Delta y^R = 2\Delta$ down to 1.3Δ, is found to reduce the amplitude of the spurious waves. This is particularly clear when the results obtained using the coarse and the medium grids in Fig. 11(a) and 11(b) are compared. Less differences are observed between the simulations performed with the medium and the refined grids in Fig. 11(b) and 11(c).

More quantitative results are given in Fig. 12 where the time evolution of the pressure difference Δp is displayed at the points A and B, located upstream the block interface and at the interface. The strongest level, obtained at the interface, is smaller than 3 Pa, corresponding to 0.3% of the pressure at the center of the vortex. In Vo-RBF-Coarsegrid, the pressure difference reaches values of 0.4 Pa and 2.9 Pa in Fig. 12(a) and Fig. 12(b). For the medium and the refined meshes, the amplitudes of the spurious waves are significantly lower than those found for the coarse grid. Indeed, in Vo-RBF-Mediumgrid, the maximum levels are close to only 0.3 Pa and 1.1 Pa. In Vo-RBF-Finegrid, a slight decrease of the pressure difference Δp is also observed compared to that in Vo-RBF-Mediumgrid, with peaks of 0.2 Pa and 0.9 Pa.

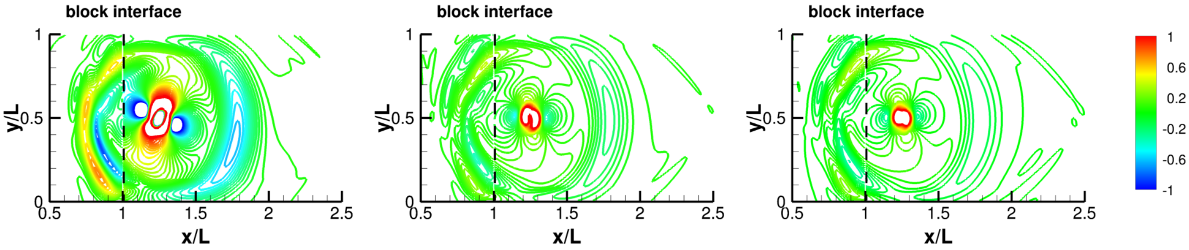

(a) (b) (c)

Fig. 11: Representation of the pressure difference Δp when the vortex is located at $x = 1.25L$: (a) Vo-RBF-Coarsegrid, (b) Vo-RBF-Mediumgrid, (c) Vo-RBF-Finegrid; levels are given in Pa.

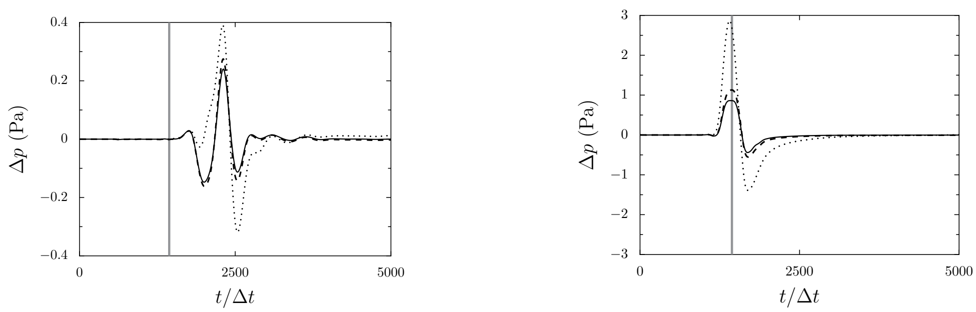

(a) (b)

Fig. 12: Representation of the time evolution of the pressure difference Δp (a) at the point A and (b) at the point B: ---- Vo-RBF-Coarsegrid, – – – Vo-RBF-Mediumgrid and —— Vo-RBF-Finegrid. The vertical grey line indicates the moment when the vortex hits the interface.

B. Mixing layer

1. *Parameters*

A two-dimensional mixing layer is simulated using the flux reconstruction technique for non-conforming grids. The flow parameters and the computational domain are identical to those considered in the simulation of Bogey and Bailly.[17] The mean longitudinal velocity profile u at the inflow at $x = 0$ is defined by the hyperbolic tangent profile:

$$u(y) = \frac{U_1 + U_2}{2} + \frac{U_2 - U_1}{2} \tanh\left(\frac{2y}{\delta_w(0)}\right) \tag{36}$$

where $U_1 = 40$ m/s and $U_2 = 160$ m/s are the low and the high flow speeds, and $\delta_w(0) = 1.6 \times 10^{-3}$ m is the initial vorticity thickness. The transverse velocity v is initially null. The flow is characterized by a Reynolds number $Re_w = \delta_w(0)(U_2 - U_1)/\nu = 1.28 \times 10^4$, where ν is the kinematic molecular viscosity. The ambient pressure is equal to 10^5 Pa. The computational domain extends from 0 down to $280\delta_w(0)$ in the streamwise direction x, and from -$320\delta_w(0)$ up to $320\delta_w(0)$ in the direction y. At the boundaries of the domain, Tam and Webb radiation conditions[18] are imposed. A Cartesian mesh, containing 441 points in each direction, is used. Upstream, in the shear layer at $x = 0$ and $y = 0$, the grid spacings in the directions x and y are equal to $\Delta x_0 = 0.32\delta_w(0)$ and $\Delta y_0 = 0.16\delta_w(0)$. The mesh is then stretched in the y-direction with a rate of 1.8% to reach $\Delta y_{max} = 3\delta_w(0)$. In the flow direction, the grid spacing is equal to Δx_0 down to $x = 110\delta_w(0)$, where a 2.8% stretching is applied in order to form a sponge zone and thus dissipate the aerodynamic fluctuations close to the outflow boundary. The mesh is splitted in two block separated by an interface located at $x = 59.5\delta_w(0)$, as depicted in Fig. 13(a). On the right side of the interface, the mesh is moved by $\Delta y_0/2$ in the transverse direction in order to create a non-conforming grid. A representation of the mesh close to the block interface is given in Fig. 13(b). Note that there is no grid discontinuity in the direction x.

The time step Δt for the computation is equal to $0.52\Delta y_0/c$, where c is the sound speed in the ambient medium. The mixing layer is excited[17] at the frequencies f_0 and $f_0/2$, where $f_0 = 0.132(U_1 + U_2)/2\delta_w(0)$. The excitation is applied at each time step at $x = 15\Delta x_0 = 4.8\delta_w(0)$ and $y = 0$. It results in the presence of vortex pairings close to $x = 60\delta_w(0)$, accompanied by the emission of acoustic waves. The vortex pairing phenomenon is visible on the vorticity field represented in Fig. 13(a). The position of the block interface appears to be close to the pairing location. Therefore, the objective is to ensure that the presence of the non-conforming grid interface does not disturb significantly the mixing layer development and the acoustic noise generated by the vortex pairings.

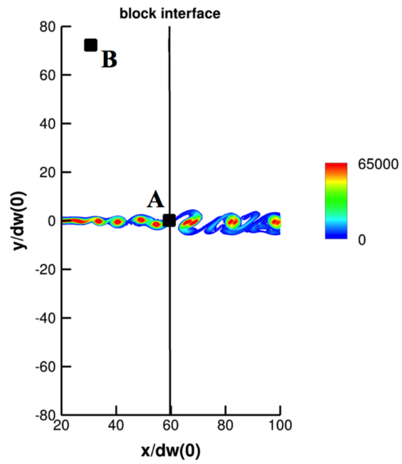

(a)

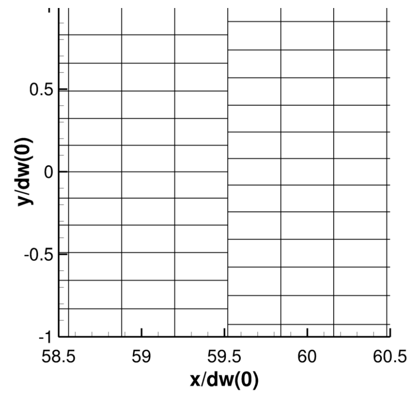

(b)

Fig. 13: Representation of (a) the vorticity field in the mixing layer with color levels between 0 and 6.5×10^4 s^{-1}; the mesh points A and B where the pressure field is recorded in the aerodynamic region at ($x = 59\delta_w(0)$, $y = 0$), and in the acoustic region at ($x = 29\delta_w(0)$, $y = 70\delta_w(0)$) are indicated by squares, (b) the mesh close to the block interface.

In this study, two simulations, denoted M-noRBF and M-RBF, are carried out. In M-RBF, the flux reconstruction at the block interface is performed with the technique based on RBF interpolations. For the interpolations, cells contained in an area defined by $n_v = 5$, and the polynomial function of degree 1 $P^T(\mathbf{x}) = (1, x, y)$ is used. In M-noRBF, the 2nd-order method previously employed for the vortex convection is applied. In order to estimate the amplitude of the spurious waves produced at the block interface, the pressure field $p_{\text{interface}}$ obtained in the multiblock simulations is compared with the pressure field $p_{\text{no-interface}}$ computed from a simulation without block interface. This reference simulation is performed using a grid coinciding with the left-hand side of the multiblock grid. The solutions of $p_{\text{interface}}$ and $p_{\text{no-interface}}$ are therefore obtained on the same grid upstream of the interface, but on different grids downstream. In the latter case, the pressure $p_{\text{no-interface}}$ is interpolated on the non-conforming grid.

Snapshots of $\Delta p = p_{\text{interface}} - p_{\text{no-interface}}$ obtained from M-noRBF and M-RBF at $t = 40000\Delta t$ are presented in Fig. 14. In the two cases, the presence of the non-conforming grid interface is responsible for pressure differences of about 10 Pa in the shear layer close to $y = 0$. Lower levels of 2-3 Pa are observed in the acoustic region for $y > 50\delta_w(0)$. The lowest levels are obtained in Fig. 14(b) in M-RBF, especially for $y > 0$ where the amplitudes of spurious waves are weaker than in M-noRBF. In the following, only the results obtained in M-RBF are presented.

In order to obtain more quantitative results concerning the mixing layer development in M-RBF, the pressure fields $p_{\text{interface}}$ and $p_{\text{no-interface}}$ are recorded at two points A and B located in the aerodynamic region close to the block interface at $x = 59\delta_w(0)$ and $y = 0$, and in the acoustic region at $x = 29\delta_w(0)$ and $y = 70\delta_w(0)$. The position of these points is indicated by squares in Fig. 13(a).

2. Pressure field in the aerodynamic region

The time variations of the pressure fluctuations $p' = p - \bar{p}$ obtained from the simulations with and without a block interface in the shear layer region at point A are given in Fig. 15(a), where $\bar{\cdot}$ represents the time-average value of the signal. The two signals are superimposed. The difference between these signals is plotted in Fig. 15(b). It reaches peaks of -18 Pa. This level is very low compared to the amplitude of the pressure fluctuations p' in Fig. 15(a), demonstrating that the presence of the non-conforming grid does not affect significantly the mixing layer development in the aerodynamic region.

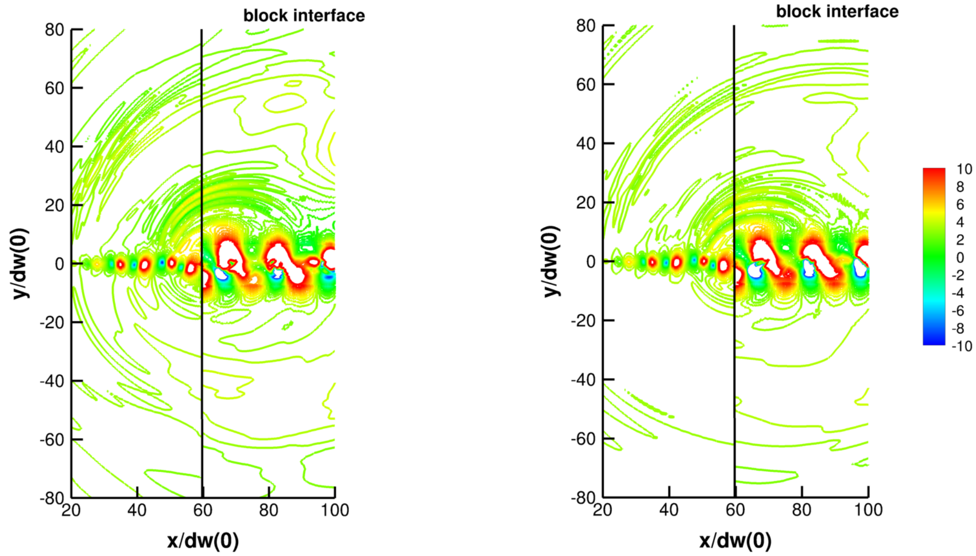

(a) (b)

Fig. 14: Representation of the pressure difference $\Delta p = p_{\text{interface}} - p_{\text{no-interface}}$ at $t = 40000\Delta t$: (a) M-noRBF and (b) M-RBF; levels given in Pa.

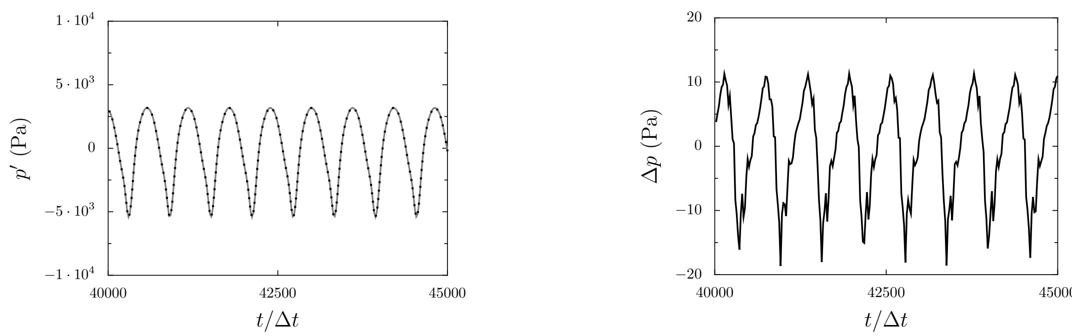

(a) (b)

Fig. 15: Representation of (a) the time evolution of the pressure fluctuations $p' = p - \bar{p}$ at point A: —— simulation without block interface and ---- M-RBF, and (b) the pressure difference $\Delta p' = p'_{\text{interface}} - p'_{\text{no-interface}}$.

3. Pressure field in the acoustic region

The pressure fluctuations p' recorded for the simulations with and without block interface in the acoustic region at point B are displayed in Fig. 16(a) . The amplitudes reach about 20 Pa. They are lower than those obtained in the shear layer. However, the signals from the two simulations are again nearly superimposed, as in Fig. 15(a). The difference between the pressure fields is plotted in Fig. 16(b). It presents a peak-to-peak value smaller than 1 Pa, which is low compared to the corresponding value of 37 Pa obtained for the pressure fluctuations p' in Fig. 16(a). These results show that the acoustic field is not significantly modified by the non-conforming grid.

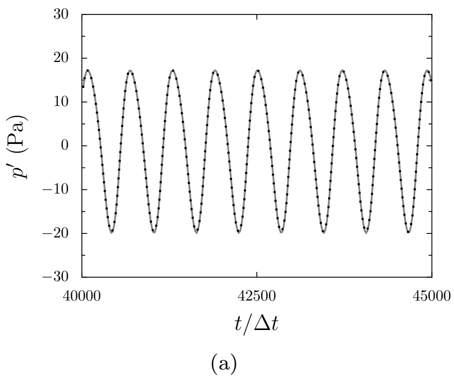

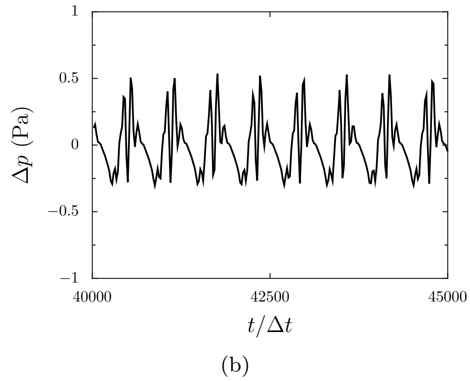

Fig. 16: Representation of (a) the time evolution of the pressure fluctuations $p' = p - \bar{p}$ at point B: —— simulation without block interface and - - - - M-RBF, and (b) the pressure difference $\Delta p' = p'_{\text{interface}} - p'_{\text{no-interface}}$.

C. Application to 3-D turbulent jet flows

In this section, the feasibility of using the flux reconstruction technique for three dimensional flows is investigated for a jet flow.

1. *Jet parameters*

A subsonic isothermal jet exiting from a pipe nozzle is computed by LES using non-conforming grid interfaces. The jet has a Mach number of $M = u_j/c = 0.6$ and a Reynolds number of $Re_D = u_jD/\nu = 5.7 \times 10^5$, corresponding to the conditions of the experiment of Cavalieri *et al.*,[19] where D and u_j are the jet diameter and velocity, c is the sound speed and ν is the kinematic molecular viscosity. The ambient pressure p_0 and temperature T_0 are equal to 10^5 Pa and 298 K. At the nozzle exit at $z = 0$, the flow is characterized by a boundary-layer thickness of $\delta = 8.5 \times 10^{-2}D$ as in the experiment.[19]

2. *Numerical parameters*

A preliminary computation at a lower cost than the computation of the full jet is carried out using a small domain. At the boundaries, Tam and Webb radiation conditions[18] are implemented. In addition, in order to weaken the hydrodynamic fluctuations at the outflow boundary, damping terms[13] and grid stretchings are applied downstream to create sponge layers. Therefore, the physical domain of the simulation extends from $z = -0.6D$ down to $z = 2.25D$ in the axial direction, and up to $r = 0.75D$ in the radial direction. Inside the nozzle, a wall model[8] developed for adiabatic walls is used to compute the boundary layer.

The axial and the radial mesh spacings Δz and Δr of the LES grid at $z = 0$, are presented in Fig. 17(a) and Fig. 17(b). In the physical domain, the mesh spacing in the axial direction is uniform and equal to $\Delta z_{min} = 0.0079D$. In the radial direction, a minimum grid spacing of $\Delta r_{min} = 0.0015D$ is imposed at the nozzle lip. From the lip, the mesh is stretched with rates lower than 8.5% in order to avoid spurious waves. In sponge zones, stretching rates greater than 10% are applied. In that way, the boundary layer thickness is discretized by about 20 points at the nozzle exit. In the azimuthal direction, 384 points are equally distributed in the jet shear layers for $r > 0.4D$ and $z < 1.5D$. Everywhere else, the number of points is halved in the azimuthal direction using non-conforming grids. Therefore, the presence of very small cells at the center of the jet is avoided.

The mesh in the $(r - \theta)$ plane at $z = 0$ is displayed in Fig. 18(a). The non-conforming grid interfaces at $r_{\text{interface}} = 0.4D$ are indicated by dashed lines. They are also visible at $z_{\text{interface}} = 1.5D$ in the $(z - r)$ plane in Fig. 18(b). The position of the interface at $r_{\text{interface}}$ is chosen such that $D/2 - r_{\text{interface}} > \delta$. For the flux reconstruction at the non-conforming-grid interfaces, the RBF interpolations are performed using areas of n_p points defined by $n_v = 4$, and the polynomial term $P^T(\mathbf{x}) = 1$.

Initially, the azimuthal and the radial velocity profiles are equal to zero, and pressure is equal to p_0. In the nozzle, the axial velocity obtained from a preliminary RANS computation is imposed and temperature is calculated using a Crocco-Busemann relation. In order to trigger the laminar-turbulent flow transition inside the nozzle, vortex rings[20] are injected in the boundary layers at $z = -0.5D$ and $r = (D - \delta)/2$ at each time step during the computation. The initialization time of the simulation corresponds to $t = 15D/c$. The

LES field is then recorded during a period of $t = 3D/c$. The statistical data thus obtained are averaged in the azimuthal direction and compared with the results of the experiment Cavalieri *et al.*[19]

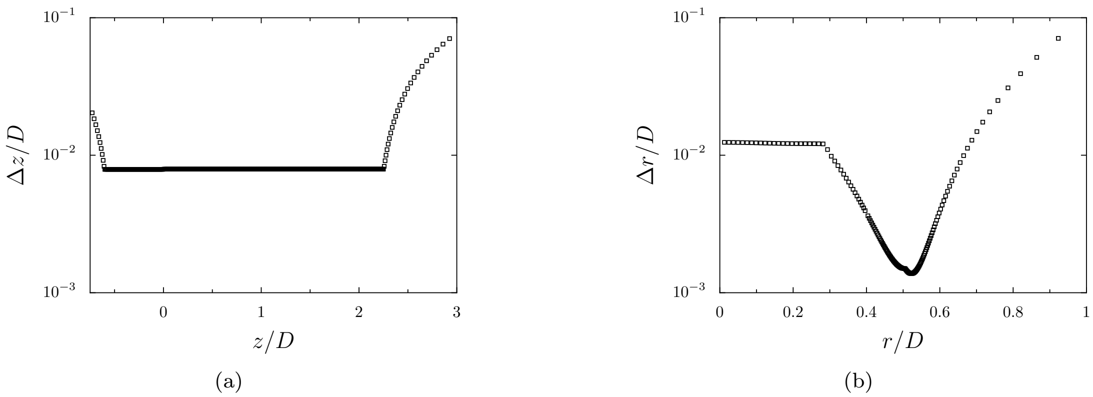

Fig. 17: Representation of the mesh spacings: (a) axial discretization $\Delta z/D$ at $r = 0$, (b) radial discretization $\Delta r/D$ at $z = 0$.

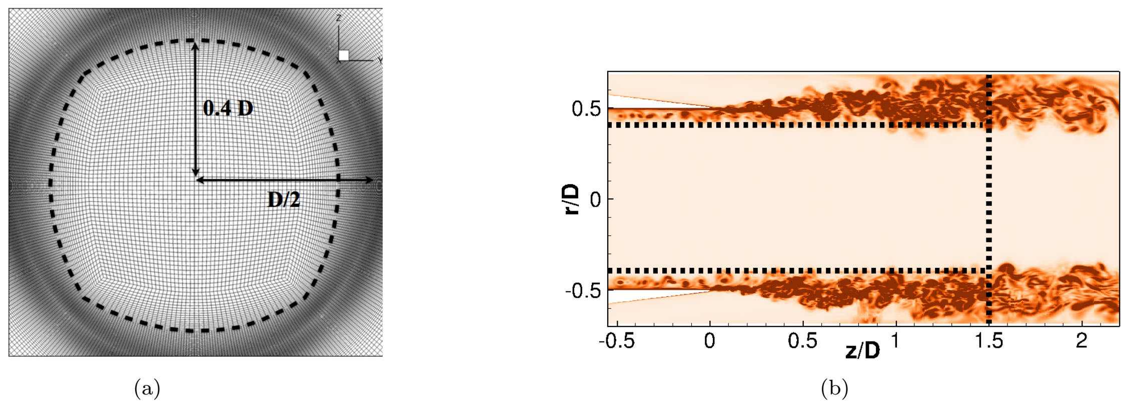

Fig. 18: Representation (a) of the mesh in the $(r - \theta)$ plane at $z = 0$, (b) of the vorticity modulus in the $(z - r)$ plane, using levels between 0 and 10 u_j/D. The non-conforming grid interfaces are represented in dashed line.

3. Results

The development of the jet close to the nozzle is illustrated in Fig. 18(b) in which a snapshot of the vorticity modulus is presented. The vortex rings injected at $z = -0.5D$ appear to result in a highly disturbed boundary layer at the nozzle exit. Downstream of the nozzle, the shear layers progressively thicken as expected. No spurious oscillations are visible close to the interfaces in dashed lines. Therefore, the presence of the non-conforming grid interfaces does not seem to affect significantly the aerodynamic development of the jet.

More quantitative results are provided in Fig. 19 where the mean and the rms axial velocities at the nozzle exit are displayed, as functions of the radial distance. The mean turbulent profile $< u_z > /u_j$ obtained from LES is comparable to the experimental data.[19] The rms axial velocity $< u'_z u'_z >^{1/2} /u_j$ at the nozzle exit is correctly estimated with a peak around 12% of the jet velocity. No numerical artifact is visible at the non-conforming interface at $r = 0.4D$ on the mean and the rms profiles.

Finally, the variations of the mean axial velocity along the lipline at $r = 0.5D$ obtained from the LES and from the experiment of Cavalieri *et al.*[19] are plotted in Fig. 20. The LES profile is in a fairly good agreement with the measurements. There is no discontinuity at the non-conforming grid interface at $z = 1.5D$.

These preliminary results show that the flux reconstruction can be applied to 3-D flows. A simulation on an extended computational domain is under progress in order to evaluate the performance of the flux reconstruction for the estimation of the aerodynamic jet development in the near-field region and of the acoustic field radiated by the jet in the far-field.

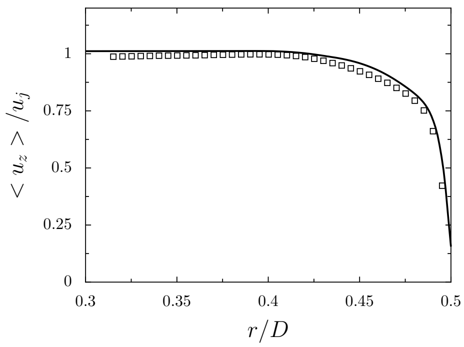

(a)

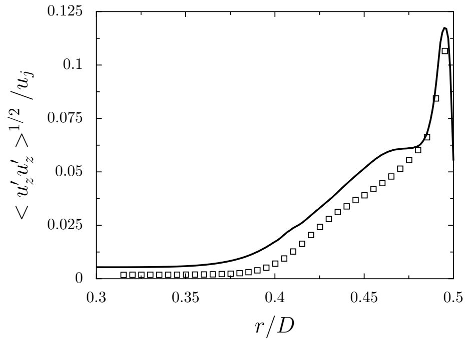

(b)

Fig. 19: Representation of (a) the mean axial velocity and (b) the rms axial velocity at the nozzle exit of the jet: —— LES, □ experiment of Cavalieri *et al.*[19]

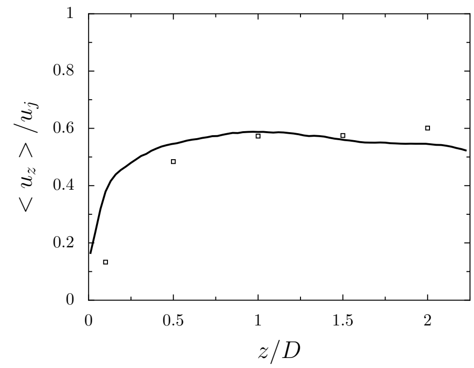

Fig. 20: Representation of the mean axial velocity at $r = 0.5D$: —— LES, □ experiment of Cavalieri *et al.*[19]

IV. Conclusions

In this paper, a flux reconstruction technique for non-conforming grid interfaces is presented in order to perform aeroacoustic simulations for multiblock structured meshes. This technique extends the application of 6th-order implicit centered schemes to non-conforming grids. It consists in using upwind schemes with ghost cells to calculate the flow variables and thus to determine the flux at the interfaces. Meshless interpolations, based on the use of radial basis functions, are carried out in order to compute the flow variables in the ghost cells. The quality of the flux reconstruction method is examined for 2-D problems, namely vortex convection and a mixing layer. The results highlight the benefit of performing radial basis interpolations with respect to the reconstruction accuracy. The amplitude of the spurious waves due to the presence of the non-conforming interface is low compared to the pressure fluctuations in the flow field. The feasibility of using the flux reconstruction technique for 3-D flows is then illustrated for a turbulent round jet flow at $Re_D = 5.7 \times 10^5$. The jet development in the vicinity of the nozzle is successfully predicted. Promising results are thus expected when simulating more complex flow configurations.

Acknowledgments

This study is financially supported by Airbus. The post-processing was performed using Antares.[21]

References

[1] JG Wang and GR Liu. A point interpolation meshless method based on radial basis functions. *International Journal for Numerical Methods in Engineering*, 54(11):1623–1648, 2002.

[2] WJ Costin and CB Allen. Numerical study of radial basis function interpolation for data transfer across discontinuous mesh interfaces. *International Journal for Numerical Methods in Fluids*, 72(10):1076–1095, 2013.

[3] L Cambier, S Heib, and S Plot. The Onera elsA CFD Software: Input from Research and Feedback from Industry. *Mechanics & Industry*, 14(03):159–174, 2013.

[4]A Fosso, H Deniau, F Sicot, and P Sagaut. Curvilinear finite volume scheme using high order compact intepolation. *Journal of Computational Physics*, 229(13):5090–5122, 2010.

[5]MR Visbal and DV Gaitonde. On the use of higher-order finite-difference schemes on curvilinear and deforming meshes. *Journal of Computational Physics*, 181:155–185, 2002.

[6]D Fauconnier, C Bogey, and E Dick. On the performance of relaxation filtering for large-eddy simulation. *Journal of Turbulence*, 14(1):22–49, 2013.

[7]F Kremer and C Bogey. Large-eddy simulation of turbulent channel flow using relaxation filtering: Resolution requirement and reynolds number effects. *Computers & Fluids*, 116:17–28, 2015.

[8]S Le Bras, H Deniau, C Bogey, and G Daviller. Development of compressible large-eddy simulations combining high-order schemes and wall modeling. In *21st AIAA/CEAS Aeroacoustics Conference, paper AIAA-2015-3135*, 2015.

[9]M Lazareff, AM Vuillot, and L Cambier. Manuel théorique du logiciel elsA, 2010.

[10]C Bogey and C Bailly. A family of low dispersive and low dissipative explicit schemes for flow and noise computations. *Journal of Computational Physics*, 194(1):194–214, 2004.

[11]A Fosso Pouangué, M Sanjosé, S Moreau, G Daviller, and H Deniau. Subsonic jet noise simulations using both structured and unstructured grids. *AIAA Journal*, 53(1):55–69, 2014.

[12]EF Toro, M Spruce, and W Speares. Restoration of the contact surface in the HLL-riemann solvers. *Shock waves*, 4(1):25–34, 1994.

[13]A Fosso. *Schémas Volumes Finis Précis: application à l'aéroacoustique numérique de jets subsoniques*. PhD thesis, Université Pierre et Marie Curie, 2011.

[14]DV Gaitonde and MR Visbal. High-order schemes for navier-stokes equations: algorithm and implementation into fdl3di. Technical report, DTIC Document, 1998.

[15]H Wendland. *Scattered data approximation*, volume 17. Cambridge University Press, 2004.

[16]MA Golberg, CS Chen, and H Bowman. Some recent results and proposals for the use of radial basis functions in the bem. *Engineering Analysis with Boundary Elements*, 23(4):285–296, 1999.

[17]C Bogey and C Bailly. Numerical Simulation of Sound Generated by a Vortex Pairing in a mixing layer. *AIAA Journal*, 38(12):2210–2218, 2000.

[18]CKW Tam and JC Webb. Dispersion-relation-preserving finite difference schemes for computational acoustics. *Journal of Computational Physics*, 107:262–281, 1993.

[19]AVG Cavalieri, P Jordan, T Colonius, and Y Gervais. Axisymmetric superdirectivity in subsonic jets. *Journal of Fluid Mechanics*, 704:388–420, 2012.

[20]C Bogey, C Bailly, and D Juvé. Noise investigation of a high subsonic, moderate Reynolds number jet using a compressible large eddy simulations. *Theoretical and Computational Fluid Dynamics*, 16(4):273–297, 2003.

[21]A Gomar, T Léonard, et al. Antares: Python Post-Processing Library, www.cerfacs.fr/antares, CERFACS, Toulouse, France, 2012.